The International Journal of Advanced Manufacturing Technology (2018) 96:2161–2173
https://doi.org/10.1007/s00170-018-1782-7

ORIGINAL ARTICLE

Optimization of cutting conditions in hard milling with the performance of cemented carbide tool material considered

Xiaobin Cui[1] · Xingshuai Zheng[1] · Jingxia Guo[2]

Received: 28 October 2017 / Accepted: 11 February 2018 / Published online: 19 February 2018

Abstract
In the present study, cutting conditions in face milling of AISI H13 hardened steel were optimized considering the performance of cemented carbide tool material. The initial microscopic mechanical property of the cemented carbide tool material was analyzed based on damage mechanics and boundary element method. Taking the initial microscopic mechanical property of the tool material, the initial macroscopic mechanical property of the tool material and external loads in the cutting process into account, a new tool life indicator was proposed. On the basis of the characteristics of tool life indicator and specific cutting energy, a theoretical method was established for the optimization of cutting conditions. The optimum cutting conditions were distinguished for different milling conditions. Feed per tooth f_z with a value around 0.2 mm/tooth and cutting speed v ranging from 150 to 250 m/min should be used in symmetric milling to acquire a relatively long tool life and relatively low energy consumption. In down milling, feed per tooth f_z should be in the range of 0.15 to 0.2 mm/tooth and cutting speed v should be between 100 and 200 m/min. Feed per tooth f_z close to 0.2 mm/tooth and cutting speed v between 200 and 300 m/min should be adopted in up milling.

Keywords Cutting conditions · Optimization method · Hard milling · Cemented carbide tool material

1 Introduction

Milling has been extensively used to manufacture critical parts in industry. Being a typical kind of milling method, face milling has been widely applied for the acquisition of surfaces with high geometric accuracy. In face milling of hardened steel, relatively severe mechanical and thermal impacts arise due to the intermittence in the cutting process and high hardness of the workpiece. Because of this, fracture tends to be the main failure mechanism of cemented carbide tool. Therefore, the cemented carbide tool life in hard milling has been a critical concern for many researchers. Taking into account environmental problems, there is growing concern about energy consumption in the manufacturing industry. Specific cutting energy can be defined as the energy required in removing a unit volume of workpiece material as reported by Shaw [1]. It can be used to characterize the energy consumption in the cutting process of face milling. Both tool life and specific cutting energy can be used to evaluate the performance of the cemented carbide tool material in face milling of hardened steel. For the purpose of maximizing the utilization of the cemented carbide tool material, tool life and specific cutting energy should be considered at the same time in the optimization of cutting conditions.

A great amount of studies [2–5] have been conducted by researchers to analyze tool lives and tool failure mechanisms in hard milling. Much valuable information can be drawn from these previous studies. However, relatively few researches [6–8] were carried out in the field of face milling of hardened steel. Ultra-high-speed face milling of hardened steel was performed by Liu et al. [6], and it was found that the main tool wear types varied as the combination of tool material and workpiece changed. The influencing mechanisms of chip formation on cutting tool edge wear were analyzed by Cui et al. [7]. Siller et al. [8] analyzed the cutting performance of a carbide tool in high-speed face milling of hardened steel. The analysis results indicated that acceptable tool lives and surface roughness Ra ranging from 0.1 to 0.3 μm can be obtained at the same time.

✉ Xiaobin Cui
kokcxb@163.com

[1] School of Mechanical and Power Engineering, Henan Polytechnic University, Jiaozuo 454003, People's Republic of China

[2] School of Energy Science and Engineering, Henan Polytechnic University, Jiaozuo 454003, People's Republic of China

It can be found from the abovementioned studies that many experimental analyses were performed to assess tool lives and investigate tool failure mechanisms. Most of the investigations of tool failure mechanisms focused on the macroscopic mechanical properties of the cutting tool material and the effects induced by external loads. The tool failure is mainly dominated by the initial state of the tool material and the external loads. The initial state of the tool material involves the microscopic and macroscopic mechanical properties of the initial tool material. Therefore, the microscopic mechanical properties of the tool material, the macroscopic mechanical properties of the tool material, and external loads should all be considered in the researches relevant to tool life and tool failure mechanisms.

There existed many valuable researches on energy consumption [9–11] in milling. However, relatively few studies [12] on specific cutting energy were carried out in the field of face milling of hardened steel. Gao et al. [12] analyzed specific cutting energy and parameter optimization in micromilling of steel. The analysis results can be used to prolong tool life and improve machining quality.

It can be concluded from the previous researches on tool life and specific cutting energy that scant studies of hard milling were conducted with both tool life and specific cutting energy considered. Tool life and specific cutting energy are two important factors in evaluation of the performance of the cemented carbide tool material. It is of great value for the efficient use of the cemented carbide tool material to explore the optimum cutting condition where relatively long tool life and relatively low specific cutting energy appear simultaneously.

In the present work, the performance of cemented carbide tool material is evaluated and predicted for the optimization of cutting conditions in face milling of AISI H13 hardened steel. Based on the analysis of the initial state of the cemented carbide tool material, a tool life indicator is proposed considering the initial microscopic mechanical properties of the tool material, the initial macroscopic mechanical properties of the tool material, and external loads in the cutting process. The tool life indicator and specific cutting energy are calculated, and characteristics of them are distinguished for different milling conditions. According to the characteristics of both tool life indicator and specific cutting energy, a theoretical method is put forward for optimizing the cutting conditions in face milling of hardened steel. The optimum cutting conditions are identified for up milling, down milling, and symmetric milling.

2 Experimental procedures and simulations

2.1 Experimental procedures

Face milling of hardened steel was conducted in the present work. Uncoated cemented carbide tools were utilized as the cutting inserts which were clamped into the face milling cutter body. The diameter of the milling cutter was 63 mm. Major cutting edge angle (κ_r) 75°, axial rake angle (γ_ρ) −6°, and radial rake angle (γ_f) −7° were provided by the milling cutter. A block of AISI H13 steel with a hardness ranging from 45 to 47 HRC was used to be the workpiece in face milling. Material properties of the cutting insert and workpiece are shown in Tables 1 and 2, respectively. All the face milling tests were performed on a CNC machining center in dry cutting condition as shown in Fig. 1.

Symmetric milling, down milling, and up milling were adopted in the milling tests. There are mainly four cutting parameters such as cutting speed, feed per tooth, radial depth of cut, and axial depth of cut. Radial depth of cut is greatly influenced by the workpiece size. Axial depth of cut is mainly dominated by technological requirements. Considering these, two other parameters, namely, cutting speed and feed per tooth, are concentrated on in this work. Radial depth of cut (a_e) and axial depth of cut (a_p) were kept the same for each kind of milling condition. a_e and a_p were set to be 30 and 0.3 mm, respectively. Cutting speed v applied in the work was in the range of 100 to 300 m/min at an interval of 50 m/min (100, 150, 200, 250, 300 m/min). Feed per tooth f_z ranging from 0.1 to 0.3 mm/z (0.1, 0.15, 0.2, 0.25, 0.3 mm/z) were utilized. It can be deduced that there existed 25 different combinations of cutting parameters for each milling condition.

In the milling experiments, each test was replicated three times. During the cutting process, the cutting forces were measured and recorded using a Kistler piezoelectric dynamometer as shown in Fig. 1. The sampling frequency of the cutting force was set as 10,000 Hz. The cutting tools in the milling tests were examined periodically using a digital microscope. The tool life was recorded when the tool flank wear reached or was larger than 0.3 mm.

2.2 Boundary element simulation and finite element simulation

A boundary element method (BEM) was utilized in the analysis of the initial state of the cemented carbide tool

Table 1 Material properties of the cutting tool

	Density (10^3 kg m^{-3})	Poisson ratio	Thermal conductivity (W m^{-1} K^{-1})	Thermal expansion (10^{-6} K^{-1})
Cutting insert	14.37	0.22	74.35	4.46

Table 2 Material properties of the workpiece

	Density (10^3 kg m^{-3})	Elastic modulus (GPa)	Poisson ratio	Thermal conductivity (W m^{-1} K^{-1})	Thermal expansion (10^{-6} K^{-1})
Workpiece	7.78	208	0.27	28.40	10.40

material. BEM is a boundary-type method, in which the partial differential equations (PDE) are transformed into integral equations called boundary integral equations (BIEs). The problems are solved based on the discretized BIEs, and the problem dimension is reduced by 1. Only the surface elements are used to discretize the boundary of model. Figure 2 shows the schematic of the three-dimensional model that was studied using the multi-domain BEM algorithm. In the present work, a representative volume element (RVE) was focused on in the analysis of the cemented carbide tool material. The grains and gas cavities of the tool material were modeled as cubes and spheres, respectively. The diameter of the sphere was equal to the length of the cube. The sizes of grain WC, binder phase Co, and gas cavity were calculated and determined according to the scanning electron microscopy (SEM) analysis of the tool material and the phase compositions of the tool material. Boundary conditions and mesh of the three-dimensional model are shown in Fig. 3. To determine Young's modulus, the RVE was stretched in the x-direction. The tensile force F_T was imposed in the x-direction, and displacement constraint was set on the RVE. In the multi-domain BEM, the domains of the grain WC and binder phase Co were discretized with the surface elements as shown in Fig. 3. Grain WC and binder phase Co were considered to be elastic. Their material properties were set on the basis of the work by Sadowski and Nowicki [13]. The elastic moduli of WC and Co were set to be 700 and 210 GPa, respectively. Their Poisson ratios were 0.24 and 0.30, respectively.

Finite element simulation of face milling was carried out to acquire cutting forces and tool stresses. Lagrangian formulation in the DEFORM-3D package was applied for the simulation. For different milling conditions such as up milling, down milling, and symmetric milling, simulation was performed for each combination of cutting parameters. Figure 4 shows the schematic of the simulation of face milling. It can be found from Fig. 4 that the geometry of the workpiece was simplified for enhancing the efficiency of simulation. The boundary conditions in the simulation were set according to the experimental setup in the milling tests. Tetrahedron elements were utilized for the mesh of cutting tool and workpiece. The contact area between the cutting tool and the workpiece was refined for both of them. During the simulation process, re-meshing technology was used for the mesh of the workpiece. For the purpose of modeling the deformation behavior of the steel under consideration, the Johnson-Cook constitutive equation was utilized and it can be defined as

$$\overline{\sigma} = \left[A + B\left(\overline{\varepsilon}\right)^{n}\right]\left[1 + C\ln\left(\dot{\overline{\varepsilon}} / \dot{\overline{\varepsilon_0}}\right)\right]\left[1 - \left(\frac{T_a - T_r}{T_m - T_r}\right)^{m}\right]. \quad (1)$$

In Eq. (1), $\overline{\sigma}$, $\overline{\varepsilon}$, $\dot{\overline{\varepsilon}}$, and T_a are employed to represent shear stress, shear strain, shear strain rate, and absolute temperature, respectively. Parameters such as yield strength (A), hardening modulus (B), strain rate sensitivity (C), strain hardening exponent (n), thermal softening coefficient (m), reference plastic strain ($\dot{\overline{\varepsilon}_0}$), reference temperature (T_r), and melting temperature (T_m) have substantial influence on the material properties of the steel. On the basis of the work by Chen et al. [14], the crucial parameters were adopted as $A = 715$ MPa, $B = 329$ MPa, $C = 0.03$, $n = 0.28$, and $m = 1.5$. The average values of resultant cutting forces in the cutting period obtained in finite element simulation (F_{as}) and milling tests (F_{at}) were compared to validate the simulation accuracy. Deviation D_e was used to evaluate the difference between F_{as} and F_{at}. D_e can be acquired using the following equation:

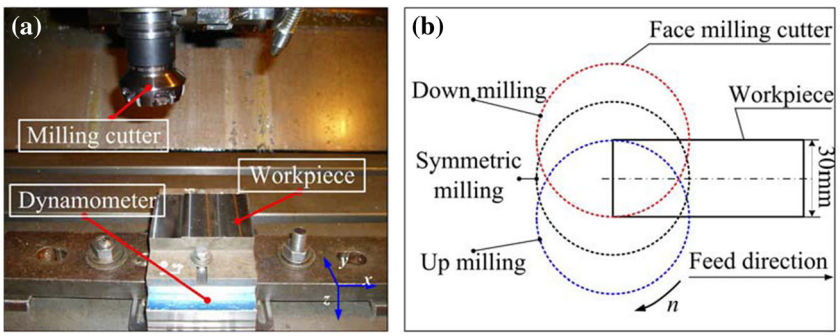

Fig. 1 Experimental setup in the milling tests

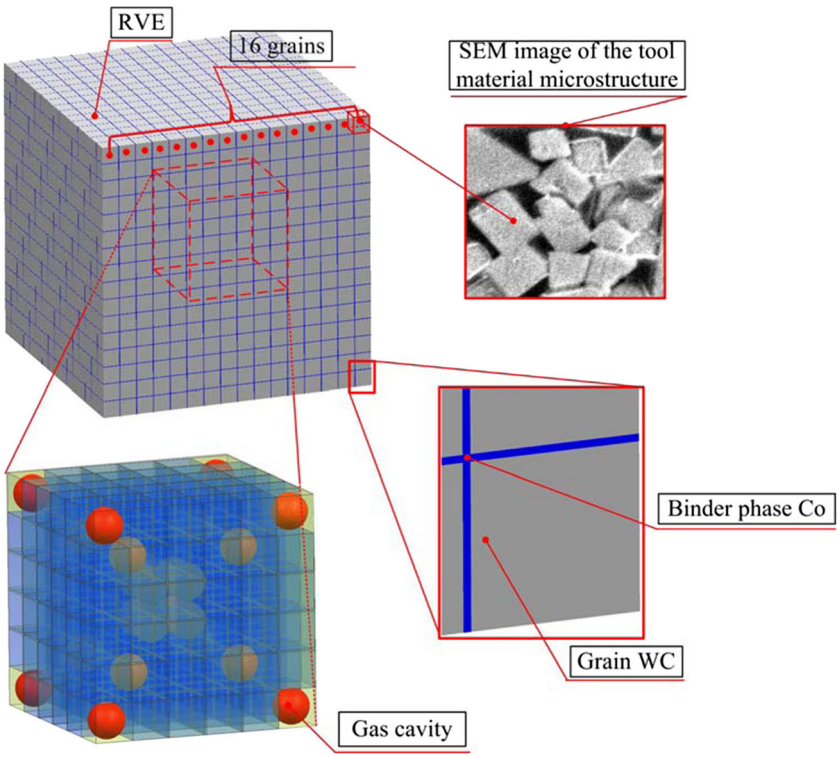

Fig. 2 Schematic of the model used in boundary element simulation

$$D_e = \frac{F_{as} - F_{at}}{F_{at}} \cdot 100\% \quad (2)$$

As an example, Fig. 5 shows the comparisons of the simulated and experimental cutting forces in symmetric milling. It can be observed from Fig. 5 that the simulated and experimental values were fairly close to each other, which demonstrates the simulation accuracy to some extent.

3 Results and discussion

3.1 Analysis of the initial microscopic mechanical property of cemented carbide tool material

In the present work, the initial microscopic mechanical property of the cemented carbide tool material was evaluated in terms of the tool material damage. The tool material damage

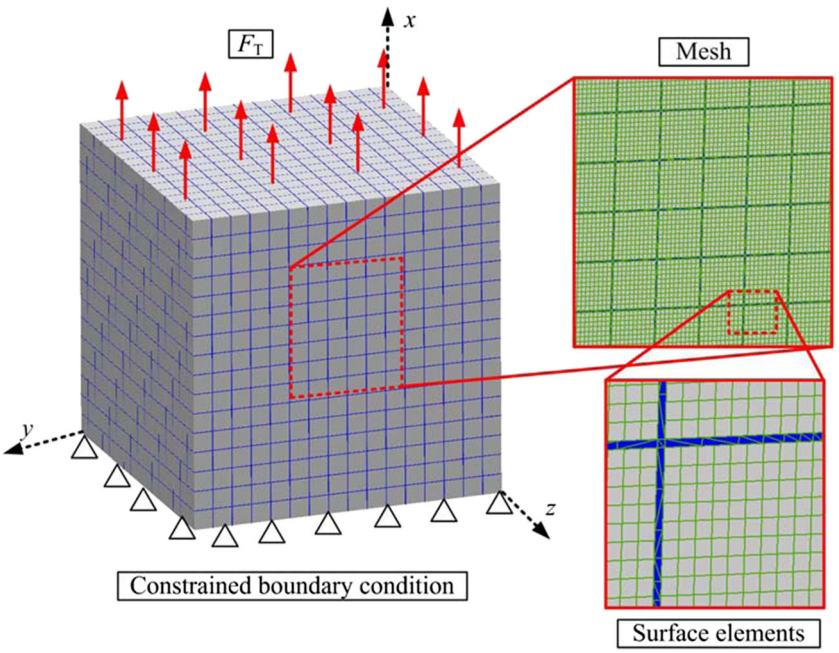

Fig. 3 Boundary conditions and mesh of the three-dimensional model

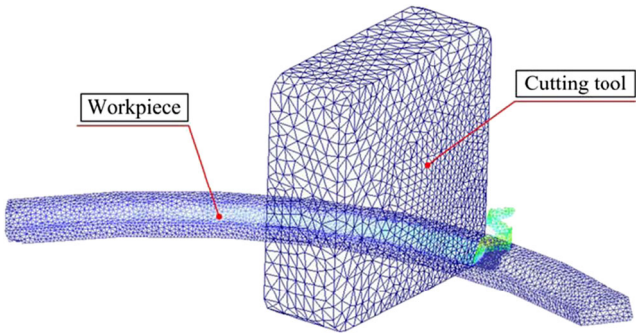

Fig. 4 Schematic of finite element simulation of face milling

was considered to be a scalar. The degradation of the elastic modulus of the tool material can be used to define the material damage as stated by Lemaitre and Lippmann [15]. The correlations between the stress σ and strain ε of the tool material without damage can be expressed as

$$\sigma = E\varepsilon \tag{3}$$

where E is the elastic modulus of the tool material with no damage. For the tool material with certain initial damage, the relationships between stress σ_d and strain ε_d can be defined as

$$\sigma_d = E_d\varepsilon_d \tag{4}$$

where E_d is the elastic modulus of the tool material with certain initial damage D_i. The following equation can be utilized to describe the relations between E, E_d, and D_i:

$$E_d = E(1-D_i) \tag{5}$$

Thus, the initial tool material damage D_i can be deduced as

$$D_i = 1-\frac{E_d}{E} \tag{6}$$

It can be inferred from Eq. (6) that E and E_d should be predetermined to acquire the value of D_i.

The material porosity has substantial effects on the elastic modulus and the initial damage of the tool material. In the present study, boundary element simulations of tensile test for the RVE shown in Fig. 2 were carried out to acquire elastic moduli of the tool material with and without gas cavities. RVE with no gas cavities was utilized in the analysis of E. E_d was obtained based on RVE with a certain amount of gas cavities.

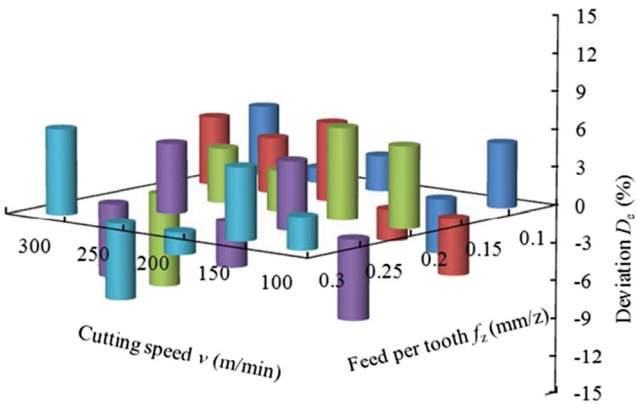

Fig. 5 Comparisons of the simulated and experimental cutting forces (symmetric milling)

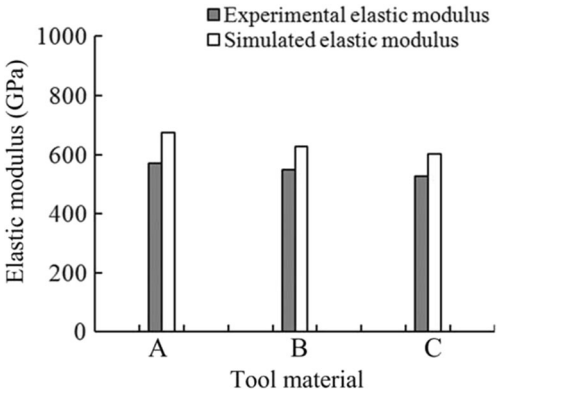

Fig. 6 Typical values of the elastic moduli obtained by means of simulation and tensile tests (tool material A: the volume fraction of cobalt was 6.3%, the tool material porosity was 1.7%, and the grain size was 1.9 μm; tool material B: the volume fraction of cobalt was 10.8%, the tool material porosity was 1.8%, and the grain size was 2 μm; tool material C: the volume fraction of cobalt was 12.2%, the tool material porosity was 2.1%, and the grain size was 2.4 μm)

In the multi-domain BEM, the boundary integral equation for each domain in RVE can be written in the following form with the absence of body forces:

$$C_{ij}u_j(P) + \int_S T_{ij}(P,Q)u_j(Q)dS(Q) = \int_S U_{ij}(P,Q)t_j(Q)dS(Q) \quad i,j = 1,2,3 \quad P,Q\in S \tag{7}$$

where $u_j(Q)$ and $t_j(Q)$ are the displacements and stress vectors at points on the boundary and $U_{ij}(P,Q)$ and $T_{ij}(P,Q)$ are fundamental solutions and can be given as following, for the three-dimensional case:

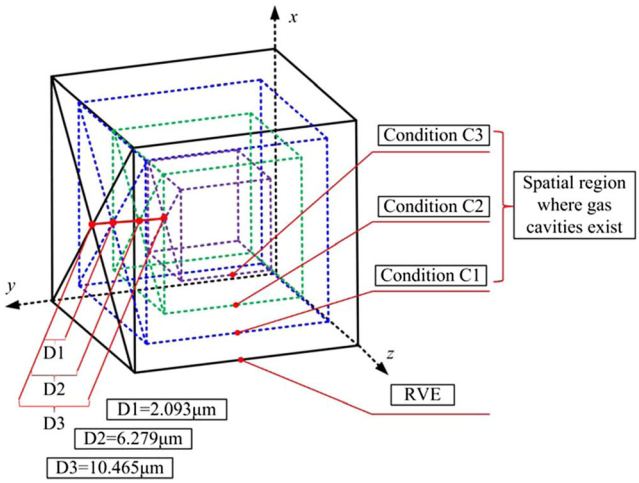

Fig. 7 Three kinds of spatial distributions of gas cavities with different clustering degrees (the volume fraction of cobalt was 10.8%, the grain size was 2 μm, and the tool material porosity was 1.2%)

$$U_{ij}(P,Q)=\frac{1}{16\pi G(1-\nu)r}\left[(3-4\nu)\delta_{ij}+r_{,i}r_{,j}\right] \tag{8}$$

$$T_{ij}(P,Q)=\frac{1}{8\pi(1-\nu)r^2}\left[\frac{\partial r}{\partial n}\left((1-2\nu)\delta_{ij}+r_{,i}r_{,j}\right)+(1-2\nu)\left(n_j r_{,i}-n_i r_{,j}\right)\right] \tag{9}$$

where G and ν are the elastic constants of the material, r represents the positional vector with its origin at point P and its end at point Q, and n is the outward normal to the boundary.

Discretizing the boundary using the linear quadrilateral elements, the discretized format of Eq. (7) can be obtained as

$$C_{ij}u_j(P)+\sum_{k=1}^{N^e}\left\{\sum_{l=1}^{M}u_j^{k,l}\int_{S^k}T_{ij}(P,Q(\xi,\eta))N_l(\xi,\eta)|J(\xi,\eta)|dS(\xi,\eta)\right\}=\sum_{k=1}^{N^e}\left\{\sum_{l=1}^{M}t_j^{k,l}\int_{S^k}U_{ij}(P,Q(\xi,\eta))N_l(\xi,\eta)|J(\xi,\eta)|dS(\xi,\eta)\right\} \tag{10}$$

where S^k represents the kth boundary element, N^e represents the total number of elements, M represents the number of nodes per element, and $u_j^{k,l}$ and $t_j^{k,l}$ are the displacement and traction components of the lth node of the kth element, respectively. In Eq. (10), the near-singular integrals should be computed accurately and efficiently when the source point P is close to but not on the surface element of integration. For modeling the composite materials, the near-singular integrals arise due to the many thin regions, such as the binder phase Co as shown in Fig. 2. The computing of the near-singular integrals can be carried out according to the studies by Cruse and Aithal [16].

With the collocation point P being placed at all nodes, the set of equations can be written as

$$\mathbf{Hu}=\mathbf{Gt}. \tag{11}$$

Considering the boundary nodes which are on the interface or not, Eq. (11) can be partitioned into blocked matrix equations as

$$\begin{bmatrix}\mathbf{H}_{BB} & \mathbf{H}_{BI}\\ \mathbf{H}_{IB} & \mathbf{H}_{II}\end{bmatrix}\begin{Bmatrix}\mathbf{u}_B\\ \mathbf{u}_I\end{Bmatrix}=\begin{bmatrix}\mathbf{G}_{BB} & \mathbf{G}_{BI}\\ \mathbf{G}_{IB} & \mathbf{G}_{II}\end{bmatrix}\begin{Bmatrix}\mathbf{t}_B\\ \mathbf{t}_I\end{Bmatrix} \tag{12}$$

where the subscripts B and I denote that the prescribed quantities are associated with the nodes on the boundary and the interface, respectively. On the boundary, either displacements or tractions (but not both) are known at every node. But the displacements and tractions ($\mathbf{u}_I$ and $\mathbf{t}_I$) are all unknown at

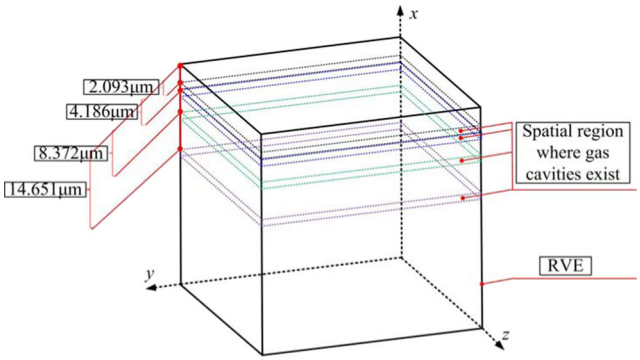

(a) Gradient distribution of gas cavities (type G1).

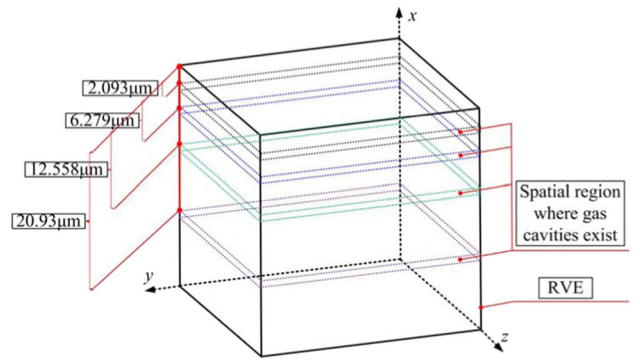

(b) Gradient distribution of gas cavities (type G2).

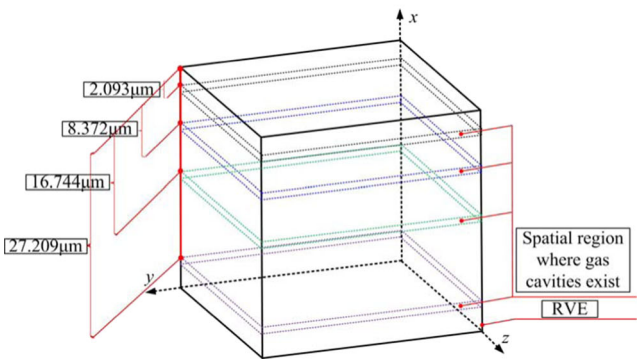

(c) Gradient distribution of gas cavities (type G3).

Fig. 8 Three different types of gradient distributions of gas cavities (the volume fraction of cobalt was 10.8%, the grain size was 2 μm, and the tool material porosity was 1.2%). **a** Gradient distribution of gas cavities (type G1). **b** Gradient distribution of gas cavities (type G2). **c** Gradient distribution of gas cavities (type G3)

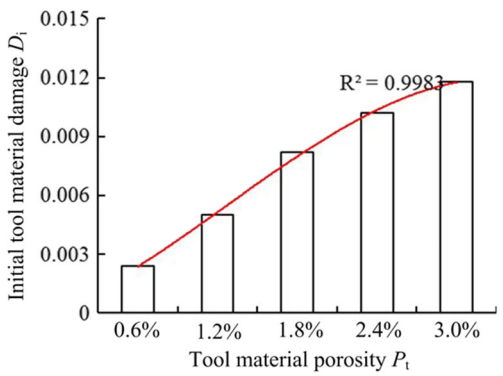

Fig. 9 The initial tool material damage D_i obtained at five different tool material porosities (the volume fraction of cobalt was 10.8%, the grain size was 2 μm)

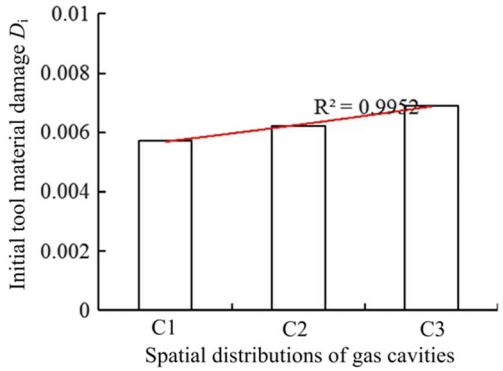

Fig. 10 The initial tool material damage D_i obtained for three kinds of spatial distributions of gas cavities with different clustering degrees (the volume fraction of cobalt was 10.8%, the grain size was 2 μm, and the tool material porosity was 1.2%)

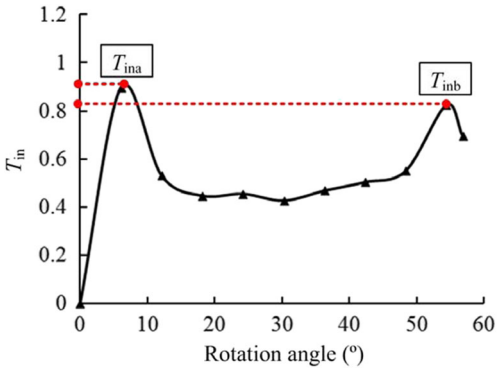

Fig. 12 The typical evolutions of tool life indicator T_{in} in cutting period (symmetric milling, $v = 200$ m/min, $a_p = 0.3$ mm, $a_e = 30$ mm, $f_z = 0.2$ mm/z)

every node on the interface. Therefore, the continuity conditions should be imposed on the interface where the displacements are identical and the tractions are equal and opposite in direction between the domains of the grain WC and binder phase Co.

Young's modulus of the RVE is estimated according to the average tensile stress and average tensile strain in the x-direction. In Eq. (10), the boundary element matrices can be obtained by computing the integrals with numerical quadrature. However, the boundary element matrices are fully populated. Computing and storing the matrices involve a numerical cost of order $O(N^2)$ which scale quadratically with respect to the degrees of freedom. Taking the computation scale of the present problem into consideration, the fast multiple method (FMM) is used to accelerate the solution of multi-domain BEM for the RVE of the cemented carbide tool material. With the FMM, the solution time and the memory requirement are reduced from order $O(N^2)$ to $O(N)$, if the iterative solver is used. The FMM for 3D elastostatic problems under consideration is performed based on previous researches by Yoshida [17].

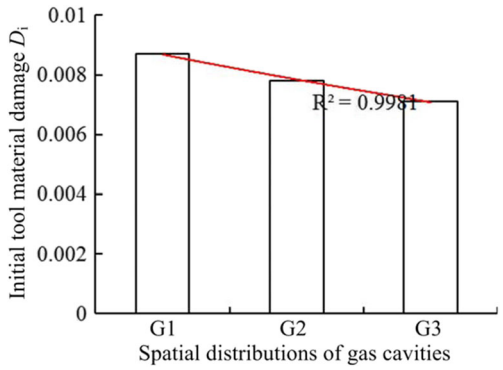

Fig. 11 The initial tool material damage D_i obtained for three different types of gradient distributions of gas cavities (the volume fraction of cobalt was 10.8%, the grain size was 2 μm, and the tool material porosity was 1.2%)

On the basis of the multi-domain boundary element method discussed above, elastic modulus (E) of the tool material without gas cavities and elastic modulus (E_d) of the tool material with certain amount of gas cavities can be obtained. The simulated and experimental values of the elastic moduli of the tool material were compared to validate the accuracy of the simulation method. Figure 6 shows several typical values of the elastic moduli obtained by means of simulation and tensile tests. The simulated elastic moduli were acquired based on a RVE with random spatial distribution of gas cavities. Figure 6 indicates that the simulated and experimental elastic moduli of the tool material were fairly close to each other. The simulated values were slightly higher than the experimental values, which can be attributed to the orderly arrangement of grains and the regular shape of grains and gas cavities in the RVE.

Based on the proposed theoretical method for the calculation of material damage, the influences of tool material porosity and spatial distributions of the gas cavities on the initial damage of the cemented carbide tool material were analyzed and identified. As for the cemented carbide tool material under consideration, the volume fraction of

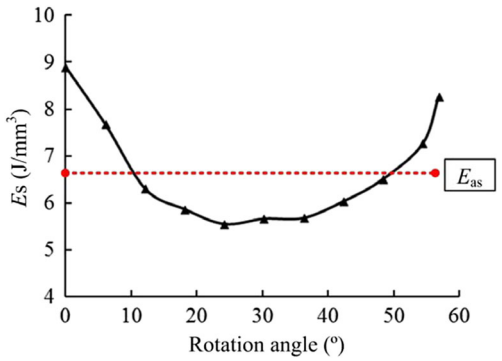

Fig. 13 The typical evolutions of specific cutting energy E_s in the cutting period (symmetric milling, $v = 200$ m/min, $a_p = 0.3$ mm, $a_e = 30$ mm, $f_z = 0.2$ mm/z)

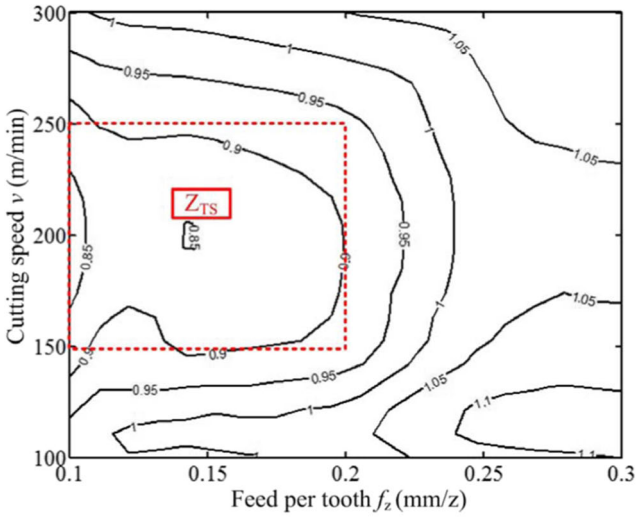

(a) T_{inm} in symmetric millling

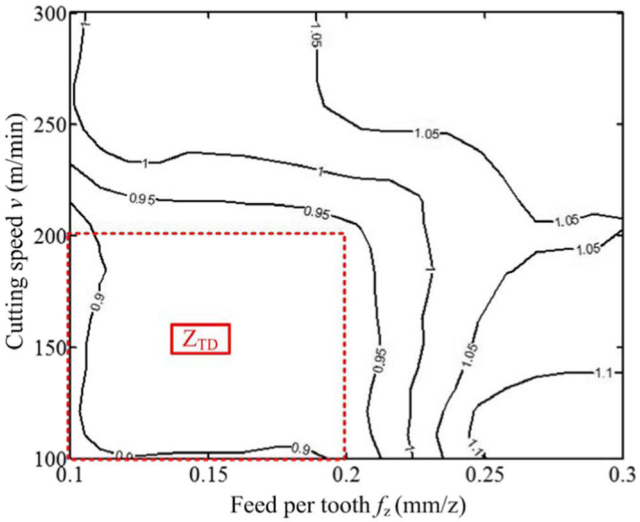

(b) T_{inm} in down millling

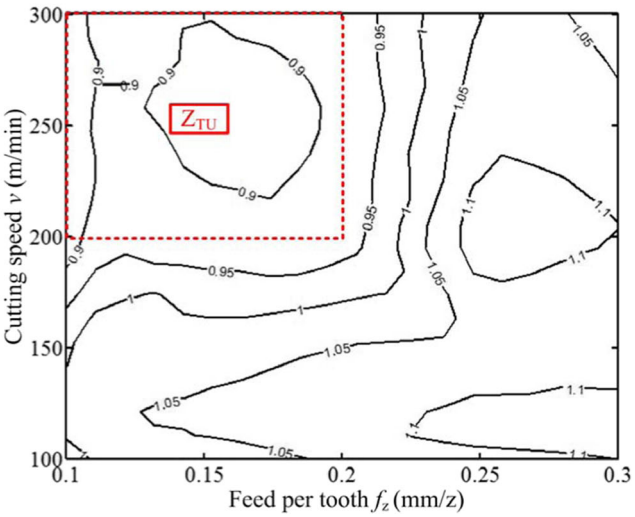

(c) T_{inm} in up millling

◀ **Fig. 14** The fitted contour maps for T_{inm} obtained under different milling conditions. **a** T_{inm} in symmetric milling. **b** T_{inm} in down milling. **c** T_{inm} in up milling

cobalt was 10.8% and the grain size was 2 μm. Five different values of tool material porosity (0.6, 1.2, 1.8, 2.4, 3%) were studied in the analysis of the effects induced by tool material porosity. In the study of tool material porosity, the gas cavities follow random spatial distribution. Clustering and gradient spatial distribution of the gas cavities were investigated when analyzing the influences caused by spatial distributions of gas cavities. Figure 7 presents three kinds of spatial distributions of gas cavities with different clustering degrees. Schematics of three different types of gradient distributions of gas cavities are shown in Fig. 8.

Figure 9 shows the initial tool material damage D_i obtained at different tool material porosities. It can be found from Fig. 9 that as tool material porosity increased from 0.6 to 3%, D_i became larger. It can also be observed that the increasing rate of D_i became lower as tool material porosity grew larger. Figure 10 shows the initial tool material damage D_i obtained for three kinds of spatial distributions of gas cavities with different clustering degrees. It can be seen from Fig. 10 that the largest value of D_i appeared when the gas cavities were of relatively high clustering degree. Figure 11 exhibits the initial tool material damage D_i acquired for three different types of gradient distributions of gas cavities. It can be observed from Fig. 11 that a relatively larger gradient of the gas cavities resulted in higher values of D_i.

3.2 Characteristics of the tool life indicator and specific cutting energy under different milling conditions

The failure of cemented carbide tool in hard milling is mainly influenced by the initial microscopic mechanical properties of the tool material, the initial macroscopic mechanical properties of the tool material, and external loads in the cutting process. These three factors should all be considered in the proposal of the tool life indicator. It has been discussed that the initial microscopic mechanical properties of the tool material were represented by the initial damage of the tool material. The effects of external loads on the cutting tool can be evaluated using tool stress in the cutting process. In the present study, tool stress was obtained by means of finite element simulation. The initial tool material damage and tool stress can be combined on the basis of the concept of damage equivalent stress, and damage equivalent stress can be used to identify the fracture of the material as indicated by Lemaitre and Desmorat [18]. Taking the initial tool material damage

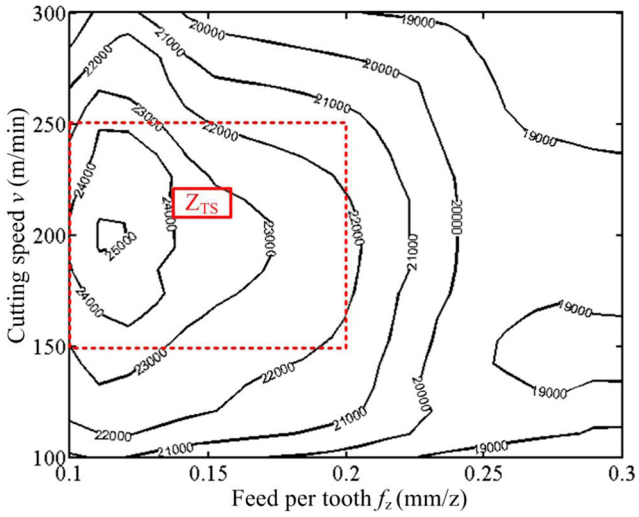

(a) N_t in symmetric millling

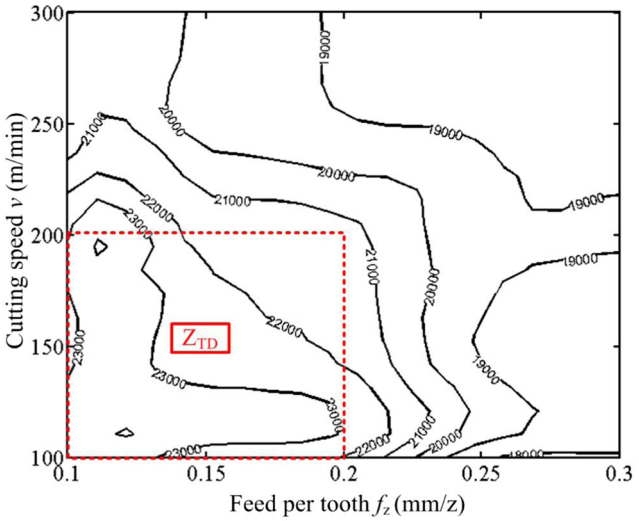

(b) N_t in down millling

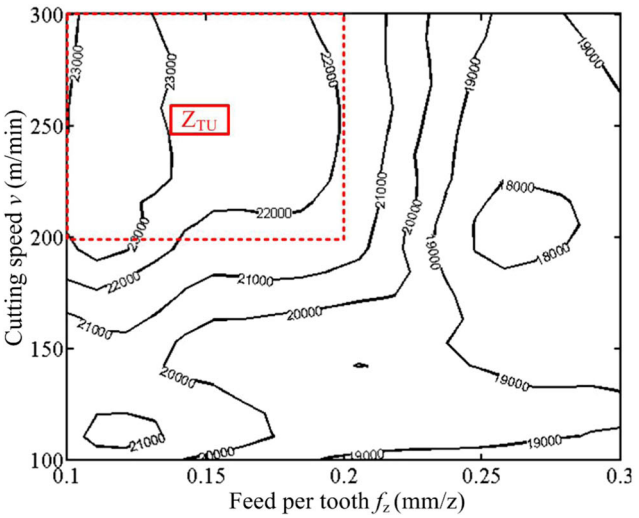

(c) N_t in up millling

◀ **Fig. 15** Experimental tool lives N_t obtained under different milling conditions. **a** N_t in symmetric milling. **b** N_t in down milling. **c** N_t in up milling

D_i and tool stress tensor $\boldsymbol{\sigma}$ into consideration, damage equivalent stress σ^* can be defined using the following equation:

$$\sigma^* = \left\{ \begin{array}{l} (1+\nu)\langle\boldsymbol{\sigma}\rangle^+ : \langle\boldsymbol{\sigma}\rangle^+ - \nu\langle \mathrm{tr}\boldsymbol{\sigma}\rangle^2 \\ + \dfrac{1-D_i}{1-hD_i}\left[(1+\nu)\langle\boldsymbol{\sigma}\rangle^- : \langle\boldsymbol{\sigma}\rangle^- - \nu\langle -\mathrm{tr}\boldsymbol{\sigma}\rangle^2\right] \end{array} \right\}^{1/2} \tag{13}$$

where ν is the Poisson ratio of the cemented carbide tool material and h is usually on the order of 0.2. Compressive strength is a critical macroscopic mechanical property of brittle and quasi-brittle materials. Compressive strength S_{com} can be used to assess the macroscopic mechanical property of the cemented carbide tool material. When the tool material was under pure compressive stress $\boldsymbol{\sigma}_c$, Eq. (13) for σ^* will change to the following form:

$$\sigma^* = \left(\frac{1-D_i}{1-hD_i}\right)^{1/2} |\boldsymbol{\sigma}_c| \tag{14}$$

Considering Eqs. (13) and (14), the value of the pure compressive stress $\boldsymbol{\sigma}_c$ can be obtained as

$$\sigma_c = \left\{ \begin{array}{l} (1+\nu)\langle\boldsymbol{\sigma}\rangle^+ : \langle\boldsymbol{\sigma}\rangle^+ - \nu\langle \mathrm{tr}\boldsymbol{\sigma}\rangle^2 \\ + \dfrac{1-D_i}{1-hD_i}\left[(1+\nu)\langle\boldsymbol{\sigma}\rangle^- : \langle\boldsymbol{\sigma}\rangle^- - \nu\langle -\mathrm{tr}\boldsymbol{\sigma}\rangle^2\right] \end{array} \right\}^{1/2} \left(\frac{1-D_i}{1-hD_i}\right)^{-1/2} \tag{15}$$

Based on Eqs. (14) and (15), a tool life indicator T_{in} can be proposed as

$$T_{in} = \frac{\sigma_{cl}}{S_{com}} = \frac{\sigma^*_{ml}\left(\frac{1-D_i}{1-hD_i}\right)^{-1/2}}{S_{com}} \tag{16}$$

where σ^*_{ml} is the largest value of damage equivalent stress σ^* in each hard milling condition. It can be found that σ_{cl} can be acquired on the basis of σ^*_{ml} and D_i. It can be inferred from the formula for tool life indicator T_{in} that a lower value of T_{in} indicates longer life of the cemented carbide tool. The value of tool life indicator T_{in} is closely related to the initial tool material damage D_i, compressive strength S_{com} of the tool material, and tool stress $\boldsymbol{\sigma}$. Therefore, it can be deduced from Eq. (16) that the effects of the initial microscopic mechanical properties of the tool material, the initial macroscopic mechanical properties of the tool material, and external loads in the cutting process on the

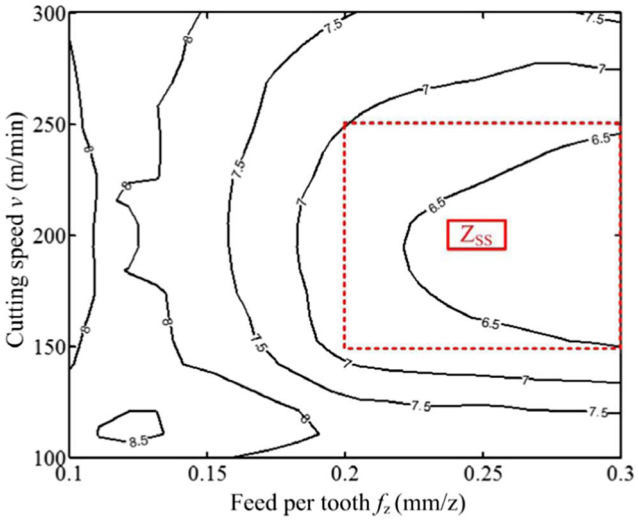

(a) E_{as} in symmetric millling

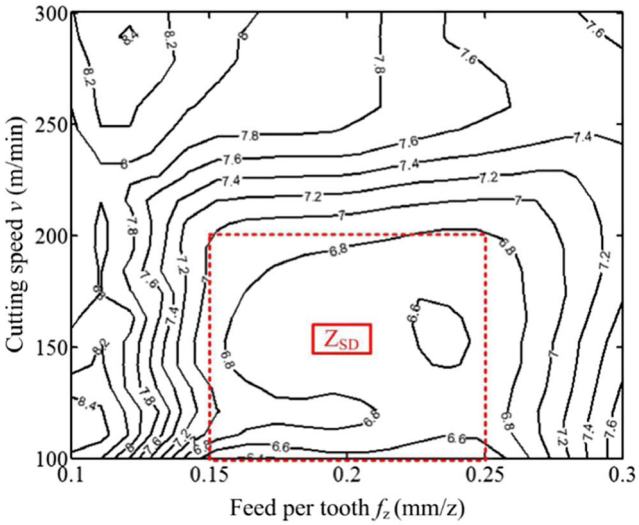

(b) E_{as} in down millling

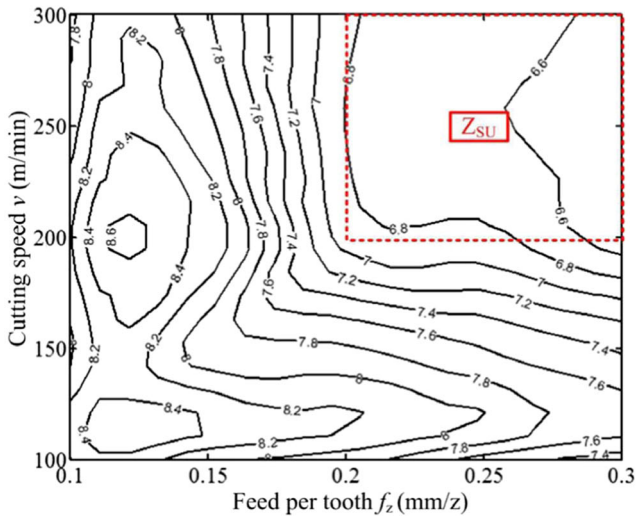

(c) E_{as} in up millling

◀ **Fig. 16** The fitted contour maps for E_{as} obtained under different milling conditions. **a** E_{as} in symmetric milling. **b** E_{as} in down milling. **c** E_{as} in up milling

cutting tool are integrated in the formula for tool life indicator T_{in}.

A specified cemented carbide tool material was used for analyzing the characteristics of the tool life indicator and specific cutting energy. Porosity of the tool material was 1.2%. The gas cavities were considered to follow random spatial distribution in the RVE. The volume fraction of cobalt was 10.8%, and the grain size was 2 μm. The initial tool material damage D_i was acquired as 0.0051. The evolutions of tool life indicator T_{in} in the cutting process can be obtained based on Eq. (16). Being an intermittent cutting process, milling contains cutting periods and non-cutting periods. The evolutions of T_{in} in cutting periods are concentrated on in the present work. It was found that when the milling condition (symmetric milling, down milling, and up milling) changed, T_{in} exhibited different evolving trends. As an example, Fig. 12 shows the typical evolution process of tool life indicator T_{in} in cutting period for symmetric milling. Figure 12 indicates that peak values of T_{in} appeared as the cutting tool cut into (T_{ina}) and cut out (T_{inb}) of the workpiece during symmetric milling. In down milling, it was found that the peak value of T_{in} arose only when the tool cut into (T_{ina}) the workpiece. Conversely, the peak value of T_{in} emerged only when the tool cut out (T_{inb}) of the workpiece in up milling. It was found that the value of T_{ina} was the largest in symmetric milling and down milling. However, in up milling, T_{inb} had the largest value. In other words, the maximum value T_{inm} of the tool life indicator was T_{ina} in symmetric milling and down milling. In up milling, the maximum value T_{inm} became T_{inb}.

Cutting speed v has a much greater value than feed rate f does in the hard milling process. Considering this, specific cutting energy E_s can be described using the following formula:

$$E_s = \frac{\Delta E_c}{\Delta V} = \frac{F_c \cdot v \cdot \Delta t}{A_c \cdot v \cdot \Delta t} = \frac{F_c}{A_c} = \frac{F_c}{a_c \cdot a_w} \left(\mathrm{J/mm^3}\right) \tag{17}$$

where E_c is the energy consumed in removing the workpiece material, V is the volume of the removed workpiece, F_c is the tangential cutting force, A_c is the area of the cutting zone, v is the cutting speed, t is the cutting time, a_c is the uncut chip thickness, and a_w is the cutting width. It can be deduced from Eq. (17) that the specific cutting energy E_s is dominated by tangential cutting force F_c, uncut chip thickness a_c, and cutting width a_w. In the present work, F_c was calculated from the simulated cutting forces. It should be noted that F_c and a_c change with the increase of cutting time t. Subsequently, specific cutting energy E_s evolves as cutting time t grows larger. It was found that the evolving trend of E_s varied as the milling

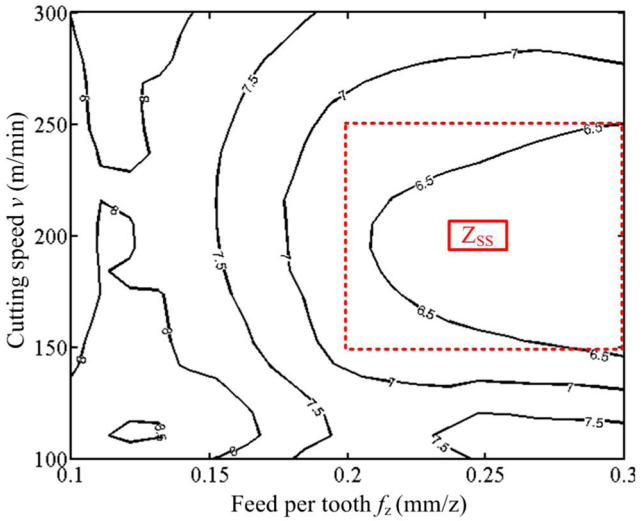

(a) E_{ase} in symmetric millling

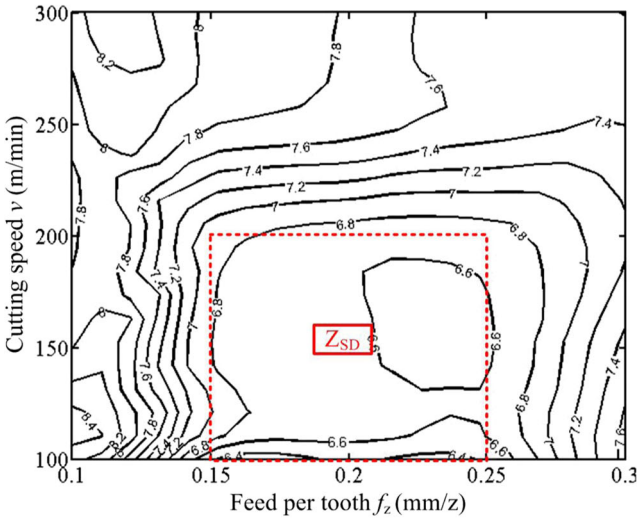

(b) E_{ase} in down millling

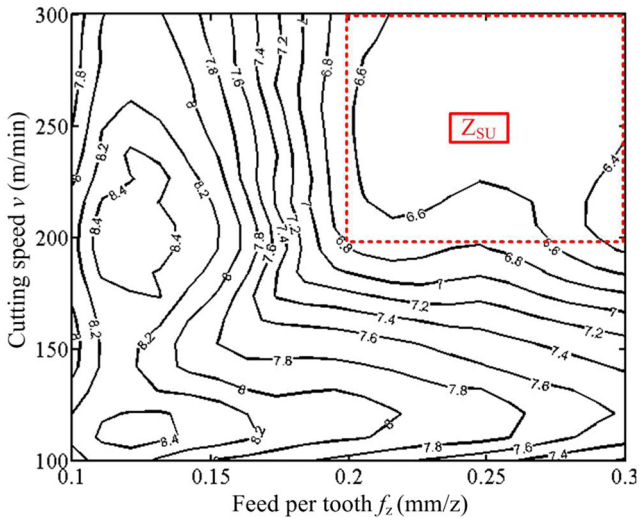

(c) E_{ase} in up millling

◀ **Fig. 17** The fitted contour maps for E_{ase} obtained under different milling conditions. **a** E_{ase} in symmetric milling. **b** E_{ase} in down milling. **c** E_{ase} in up milling

condition changed. As an example, Fig. 13 presents the typical evolutions of specific cutting energy E_s in the cutting period for symmetric milling. In symmetric milling, relatively large values of E_s arose when the cutting tool cut into and cut out of the workpiece. The value of E_s is relatively large as the cutting tool cut out of the workpiece in down milling. In contrast, the largest value of E_s appeared when the cutting tool was cutting into the workpiece during up milling. In the present work, the average value E_{as} of specific cutting energy E_s was calculated for different milling conditions.

3.3 Optimization of the cutting conditions in face milling

Based on the studies of the performance of cemented carbide tool material in face milling of hardened steel, a theoretical method can be put forward to compare and optimize the cutting conditions. First, the initial microscopic mechanical property of the cemented carbide tool material can be analyzed to determine the initial tool material damage. Then, for different milling conditions and different combinations of cutting parameters, the values of the tool life indicator can be calculated on the basis of the initial tool material damage, compressive strength of the tool material, and tool stress. The specific cutting energy can also be obtained for these milling conditions and cutting parameter combinations. The cross-cutting parameter area where relatively low values of tool life indicator and specific cutting energy emerge at the same time can be distinguished. Finally, this cross-cutting parameter area can be considered as the optimum cutting condition where relatively long tool life and relatively low energy consumption can be acquired at the same time.

Figure 14 shows the fitted contour maps for T_{inm} (the maximum tool life indicator in the cutting period) obtained under different milling conditions. It can be seen from Fig. 14 that when the milling condition varied, relatively low values of T_{inm} can be acquired in different cutting parameter areas (Z_{TS}, Z_{TD}, and Z_{TU}). Feed per tooth f_z which is between 0.1 and 0.2 mm/tooth should be adopted to obtain a lower value of T_{inm}. For the purpose of acquiring relatively low T_{inm}, cutting speed v ranging from 150 to 250 m/min should be used in symmetric milling. In down milling, cutting speed v should be in the range of 100 to 200 m/min. In up milling, cutting speed v should be between 200 and 300 m/min.

The experimental tool lives were represented by cutting cycles N_t in the present work. The experimental tool lives N_t obtained in milling tests were compared to the values of T_{inm} for different milling conditions as shown in Fig. 15. The

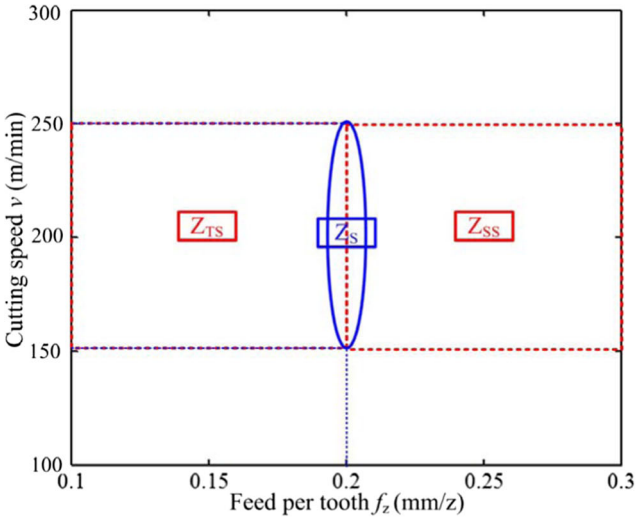

(a) The optimum cutting parameter area Z_S in symmetric millling

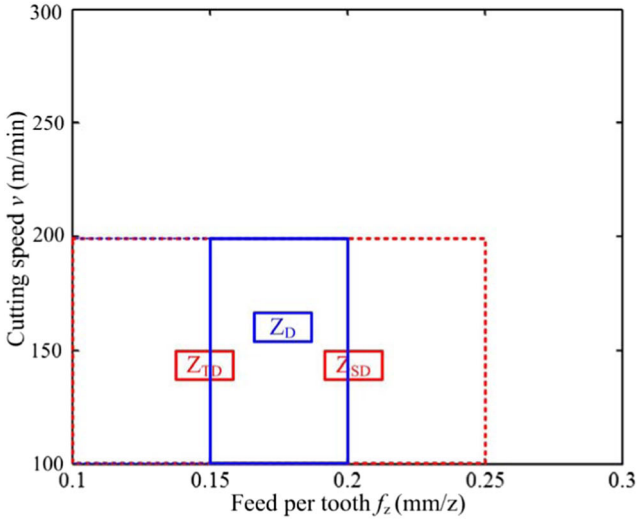

(b) The optimum cutting parameter area Z_D in down millling

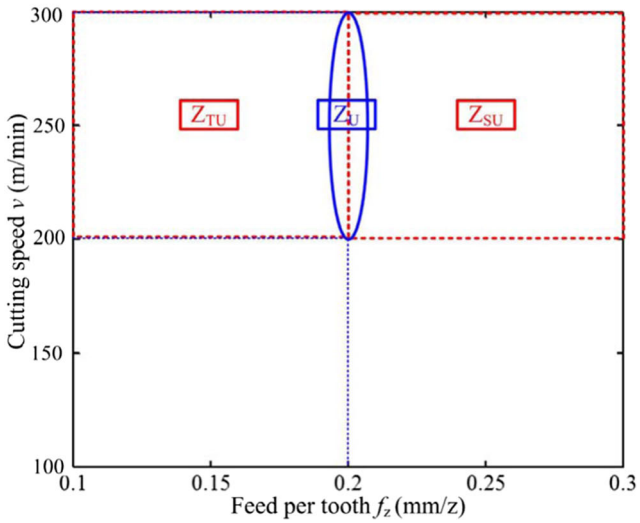

(c) The optimum cutting parameter area Z_U in up millling

◀ **Fig. 18** The cutting parameter area where relatively low values of tool life indicator and specific cutting energy arose. **a** The optimum cutting parameter area Z_S in symmetric milling. **b** The optimum cutting parameter area Z_D in down milling. **c** The optimum cutting parameter area Z_U in up milling

values of T_{inm} were relatively low in cutting parameter areas Z_{TS}, Z_{TD}, and Z_{TU}. It can be found from Fig. 15 that relatively longer tool lives arose in these areas. This validated the correctness of the use of T_{inm} as a tool life indicator.

Figure 16 presents the fitted contour maps for E_{as} (the average specific cutting energy in the cutting period) obtained under different milling conditions. When milling condition changed, relatively low values of E_{as} appeared in different cutting parameter areas (Z_{SS}, Z_{SD}, and Z_{SU}). It can be found from Fig. 16 that when feed per tooth f_z was in the range of 0.2 to 0.3 mm/tooth and cutting speed v adopted was between 150 and 250 m/min, relatively low E_{as} appeared in symmetric milling. When feed per tooth f_z stays in the range of 0.15 to 0.25 mm/tooth and cutting speed v was between 100 and 200 m/min, relatively low E_{as} arose in down milling. In order to acquire relatively low E_{as} in up milling, feed per tooth f_z should be in the range of 0.2 and 0.3 mm/tooth and cutting speed v should be between 200 and 300 m/min.

It can be seen from Eq. (17) that specific cutting energy is mainly determined by cutting force when the cutting parameters are specified. It has been shown in Fig. 5 that the simulated cutting forces which were used for the calculation of E_{as} were close to the experimental values. Therefore, the values of specific cutting energy E_{as} acquired based on simulation should be reliable. For the purpose of further demonstrating the accuracy of E_{as}, specific cutting energy E_{ase} were obtained on the basis of experiments as shown in Fig. 17. The values of E_{as} were relatively low in cutting parameter areas such as Z_{SS}, Z_{SD}, and Z_{SU}. It can be found from Fig. 17 that relatively low E_{ase} also appeared in these areas. This demonstrated the accuracy of the values of E_{as}.

Figure 18 shows the cross-cutting parameter areas where relatively low values of tool life indicator and specific cutting energy emerged for different milling conditions. Relatively long tool life and relatively low energy consumption are expected to be obtained at the same time in these cross-cutting parameter areas. The optimum cutting parameter areas for symmetric milling, down milling, and up milling were represented by Z_S, Z_D, and Z_U, respectively. When symmetric milling was applied, feed per tooth f_z with a value around 0.2 mm/tooth and cutting speed v in the range of 150 to 250 m/min should be adopted. In down milling, feed per tooth f_z should be between 0.15 and 0.2 mm/tooth and cutting speed v ranging from 100 to 200 m/min should be used. Feed per tooth f_z close to 0.2 mm/tooth and cutting speed v which is in the range of 200 to 300 m/min should be applied in up milling.

4 Conclusions

Taking the performance of cemented carbide tool material into consideration, studies of the optimization of cutting conditions in hard milling were conducted in the present work. The following conclusions can be drawn based on the present work:

1. The initial damage of the cemented carbide tool material was obtained based on damage mechanics and the multi-domain boundary element method. The initial tool material damage increased with the tool material porosity. When the tool material porosity grew larger, the increasing rate of the initial tool material damage became lower. Larger values of the initial tool material damage arose when the gas cavities were of relatively high clustering degree. Relatively larger gradient of the gas cavities led to higher values of the initial tool material damage.
2. In symmetric milling, peak values of the tool life indicator appeared when the cutting tool cut into and cut out of the workpiece. The peak value of the tool life indicator arose as the tool cut into the workpiece during down milling. In contrast, the peak value of the tool life indicator emerged when the tool cut out of the workpiece in up milling. The maximum value of the tool life indicator appeared when the tool cut into the workpiece in symmetric milling and down milling. In up milling, the maximum value arose as the tool cut out of the workpiece. In symmetric milling, relatively large specific cutting energy emerged when the tool cut into and cut out of the workpiece. The value of specific cutting energy is relatively large as the tool cut out of the workpiece in down milling. Conversely, the largest value of specific cutting energy appeared when the cutting tool was cutting into the workpiece during up milling.
3. For the purpose of acquiring relatively long tool life and relatively low energy consumption, feed per tooth f_z with a value close to 0.2 mm/tooth and cutting speed v ranging from 150 to 250 m/min should be applied in symmetric milling. In down milling, feed per tooth f_z between 0.15 and 0.2 mm/tooth and cutting speed v in the range of 100 to 200 m/min should be applied. Feed per tooth f_z about 0.2 mm/tooth and cutting speed v which is in the range of 200 to 300 m/min should be adopted in up milling.

Acknowledgements This project is supported by the National Natural Science Foundation of China (Grant Nos. 51505132 and 11602079).

References

1. Shaw MC (1997) Metal cutting principles. Clarendon Press, Oxford
2. Toh CK (2006) Cutter path orientations when high-speed finish milling inclined hardened steel. Int J Adv Manuf Technol 27(5–6):473–480
3. Wang C, Xie Y, Qin Z, Lin H, Yuan Y, Wang Q (2015) Wear and breakage of TiAlN- and TiSiN-coated carbide tools during high speed milling of hardened steel. Wear 336:29–42
4. Ghani JA, Choudhury IA, Masjuki HH (2004) Wear mechanism of TiN coated carbide and uncoated cermets tools at high cutting speed applications. J Mater Process Technol 153–154(1–3):1067–1073
5. Saketi S, Sveen S, Gunnarsson S, M'Saoubi R, Olsson M (2015) Wear of a high cBN content PCBN cutting tool during hard milling of powder metallurgy cold work tool steels. Wear 332:752–761
6. Liu Z, Ai X, Zhang H, Wang Z, Wan Y (2002) Wear patterns and mechanisms of cutting tools in high-speed face milling. J Mater Process Technol 129(1–3):222–226
7. Cui X, Zhao B, Jiao F, Zheng J (2016) Chip formation and its effects on cutting force, tool temperature, tool stress, and cutting edge wear in high- and ultra-high-speed milling. Int J Adv Manuf Technol 83(1–4):55–65
8. Siller HR, Vila C, Rodriguez CA, Abellán JV (2009) Study of face milling of hardened AISI D3 steel with a special design of carbide tools. Int J Adv Manuf Technol 40(1–2):12–25
9. Sealy MP, Liu ZY, Zhang D, Guo YB, Liu ZQ (2016) Energy consumption and modeling in precision hard milling. J Clean Prod 135:1591–1601
10. Liu ZY, Guo YB, Sealy MP, Liu ZQ (2016) Energy consumption and process sustainability of hard milling with tool wear progression. J Mater Process Technol 229:305–312
11. Yoon HS, Lee JY, Kim MS, Ahn SH (2014) Empirical power-consumption model for material removal in three-axis milling. J Clean Prod 78:54–62
12. Gao S, Pang S, Jiao L, Yan P, Luo Z, Yi J, Wang X (2017) Research on specific cutting energy and parameter optimization in micro-milling of heat-resistant stainless steel. Int J Adv Manuf Technol 89(1–4):191–205
13. Sadowski T, Nowicki T (2008) Numerical investigation of local mechanical properties of WC/Co composite. Comput Mater Sci 43(1):235–241
14. Chen L, El-Wardany TI, Nasr M, Elbestawi MA (2006) Effects of edge preparation and feed when hard turning a hot work die steel with polycrystalline cubic boron nitride tools. CIRP Ann Manuf Technol 55(1):89–92
15. Lemaitre J, Lippmann H (1992) A course on damage mechanics. Springer, Berlin
16. Cruse TA, Aithal R (1993) Non-singular boundary integral equation implementation. Int J Numer Methods Eng 36(2):237–254
17. Yoshida K (2001) Applications of fast multipole method to boundary integral equation method. Kyoto University, PhD Dissertation
18. Lemaitre J, Desmorat R (2005) Engineering damage mechanics: ductile, creep, fatigue and brittle failures. Springer, Berlin